catalysts

Article

One Stone Two Birds: Utilization of Solar Light for Simultaneous Selective Phenylcarbinol Oxidation and H_2 Production over 0D/2D-3D Pt/In_2S_3 Schottky Junction

Huijun Zhang [1,†], Peipei Xiao [1,†], Sugang Meng [1,2,*], Baihua Long [3], Qing Liu [1], Xiuzhen Zheng [1,2,*], Sujuan Zhang [1], Zhaohui Ruan [1] and Shifu Chen [1,*]

1 Key Laboratory of Green and Precise Synthetic Chemistry and Applications, Ministry of Education, College of Chemistry and Materials Science, Huaibei Normal University, Huaibei 235000, China
2 State Key Laboratory of Photocatalysis on Energy and Environment, Fuzhou University, Fuzhou 350116, China
3 College of Material and Chemical Engineering, Pingxiang University, Pingxiang 337055, China
* Correspondence: mengsugang@126.com (S.M.); zhengxz@chnu.edu.cn (X.Z.); chshifu@chnu.edu.cn (S.C.); Tel.: +86-561-3802235 (S.M.)
† These authors contributed equally to this work.

Abstract: Precise regulation and control solar-light-driven charges photoexcited on photocatalysts for separation-transfer and target redox reactions is an attractive and challenging pathway toward sustainability. Herein, 0D/2D-3D Pt/In_2S_3 Schottky junction was fabricated for simultaneous selective phenylcarbinol conversion into value-added aldehydes and production of clean energy H_2 by directly utilizing photoexcited holes and electrons in one reaction system under mild reaction conditions. In contrast to pure water splitting and pure In_2S_3, the reaction thermodynamics and kinetics of H_2 evolution on the Pt/In_2S_3 were significantly enhanced. The optimized 0.3% Pt/In_2S_3 exhibited the highest and most stable photocatalytic activity with 22.1 mmol g^{-1} h^{-1} of H_2 production rate and almost 100% selectivity of benzaldehyde production. Notably, this dual-function photocatalysis also exhibited superiority in contrast to sacrificial-agent H_2 evolution reactions such as lactic acid, Na_2S, methanol and triethanolamine. The turnover frequency (TOF) could reach up to ~2394 h^{-1}. The Pt clusters anchored at the electron location and strong metal-support interactions (SMSI) between Pt and In_2S_3 synergistically improved the spatial charge separation and directional transportation (~90.1% of the charge transport efficiency could be achieved over the Pt/In_2S_3 hybrid), and thus result in significant enhancement of photocatalytic H_2 evolution with simultaneous benzaldehyde production.

Keywords: photocatalytic H_2 production; selective oxidation; 2D nanosheets; photocatalytic organic synthesis; metal-support interactions

Citation: Zhang, H.; Xiao, P.; Meng, S.; Long, B.; Liu, Q.; Zheng, X.; Zhang, S.; Ruan, Z.; Chen, S. One Stone Two Birds: Utilization of Solar Light for Simultaneous Selective Phenylcarbinol Oxidation and H_2 Production over 0D/2D-3D Pt/In_2S_3 Schottky Junction. *Catalysts* **2023**, *13*, 461. https://doi.org/10.3390/catal13030461

Academic Editor: Weilin Dai

Received: 30 January 2023
Revised: 15 February 2023
Accepted: 20 February 2023
Published: 22 February 2023

1. Introduction

Since Fujishima and Honda reported electrochemical photolysis of water for hydrogen (H_2) production at a TiO_2 electrode in 1972 [1], photocatalytic H_2 production (PHP), as one of the most promising strategies to address the severe issues of environment and energy, has attracted extensive and ongoing attention [2–5], because PHP can be driven by inexhaustible solar energy and the reaction conditions are not as rigorous as traditional industrial methods such as coal gasification and electrolytic processes [3–7]. For instance, 15,364 scientists from 184 countries made a joint appeal to humans in 2017: "World Scientists' Warning to Humanity: A Second Notice". One of the noteworthy appeals was sustainable development [8]. Clean energy instead of fossil fuels is ineluctable in the future. More recently, European Union and other countries have made incentive schemes for green hydrogen fuel. However, PHP faces many challenges for practical application [9–12]. Two critical points are the design of efficient photocatalysts with high and stable quantum efficiency and the enhancement of output-input ratio. For photocatalytic overall water splitting into hydrogen (H_2) and oxygen (O_2), a lot greater than zero of the Gibbs free energy change and the sluggish oxidation half-reaction both make PHP hard in terms of thermodynamics and kinetics [12–14]. Although sacrificial-reagent PHP is in favor of improvements of both reaction thermodynamics and kinetics, sacrificial reagents simultaneously bring waste of the photoexcited holes, the increase in cost and the burden on the environment such as emissions of greenhouse-gas, inorganic salt and organic pollutants [14–16]. Moreover, the charge carrier recombination is still one of the challenging limitations for the photocatalysis technologies [17–24]. Recently, PHP coupled with organics transformation has held great attention [25–30]. In this dual-function photoredox reaction system, not only can the photoexcited electrons be utilized for reducing H^+/H_2O into H_2, the photoexcited holes can also be used for oxidizing organics into fine chemicals. For instance, aromatic aldehydes and H_2 can be simultaneously obtained by the photocatalytic splitting of aromatic alcohols in one reaction system [31–33]. However, the photocatalysts suitable for this dual-function photoredox reaction system with efficient reaction kinetics still need to be explored.

To drive this dual-function photoredox reaction, choosing photocatalysts with a proper band gap and suitable band positions is the initial step. Among various photocatalysts, low-dimensional metal sulfides showed tremendous potential for this dual-function photoredox reaction because of their appealing optical–electrical characteristics and appropriate band structures [34–36]. However, metal sulfides used as photocatalysts still face various problems: low utilization of visible light, photocorrosion and recommendation of photoexcited charge carriers, which significantly inhibit its reaction kinetics and stability [37–39]. To address the problems, many approaches have been developed such as doping [40,41], noble-metal deposition [30,42,43], cocatalysts [5,31,44] and heterojunction composites [45–47]. After modification, the photocatalytic activity and stability of the pristine metal sulfides ($Zn_3In_2S_6$, CdS, $Zn_xCd_{1-x}S$ and $ZnIn_2S_4$) both are improved. However, precise regulation and control solar-light-driven charges photoexcited on photocatalysts for separation-transfer and target redox reactions is still a challenge.

Herein, 0D/2D-3D Pt/In_2S_3 heterostructure was prepared by sequential hydrothermal-photodeposition methods and was applied for PHP with simultaneously selective phenylcarbinol conversion under simulated sunlight irradiation. In the previous study, In_2S_3 exhibited potential applications in photocatalytic pollutant degradation [48], selective oxidation [49,50], H_2 production [22–24], etc. It may have been an alternative photocatalyst for this dual-function photoredox reaction. In addition, In_2S_3 possesses smaller band-gap energy (~2.0 eV) [51] than $Zn_3In_2S_6$ (~2.9 eV) [14], CdS (~2.4 eV) [52,53], $Zn_{0.5}Cd_{0.5}S$ (~2.6 eV) [45] and $ZnIn_2S_4$ (~2.4 eV) [31,54], suggesting more and broad light absorption. The 0D/2D-3D Pt/In_2S_3 hierarchical structure has the following advantages: 2D nanosheets and 3D spheres of In_2S_3 hierarchical structure facilitate light harvesting via multi-layer reflection, 0D Pt deposition and close contact, and sedimentary separation from the reaction system. On the other hand, the exposed 0D Pt clusters can make full use of Pt atoms and save costs. Therefore, the 0D/2D-3D hierarchical structure is significant for PHP. Moreover, it has been demonstrated that the Schottky junction can improve charge separation [55]. In this study, 0D Pt clusters were anchored at the separated electron location of In_2S_3 by an in situ photoreduction process. The formed Pt/In_2S_3 Schottky junction coupled with strong metal–support interactions (SMSI) between 0D Pt clusters and 2D In_2S_3 nanosheets can improve the electron separation and transportation from In_2S_3 into Pt for PHP and reserve the holes at In_2S_3 for selective oxidation of phenylcarbinol, and thus result in significant enhancement of PHP with almost 100% selectivity of benzaldehyde production. Notably, benzaldehyde is important for chemical raw material, methylene reagents, perfume, herbicide intermediates, etc. In addition, the as-prepared 0D/2D-3D Pt/In_2S_3 heterostructure exhibits superiority for PHP coupled with phenylcarbinol in contrast to sacrificial agents such as lactic acid, Na_2S, methanol and triethanolamine. Moreover, the photocatalytic mechanism was also studied profoundly by several recognized techniques such as the photoelectrochemical (PEC) test, in situ electron paramagnetic resonance (EPR) and in situ diffuse reflectance infrared Fourier transform spectroscopy (DRIFT), etc.

2. Results and Discussion

2.1. Catalysts Characterization

The micro-structures of 2D-3D In_2S_3 and 0D/2D-3D Pt/In_2S_3 were characterized by scanning electron microscope (SEM), transmission electron microscope (TEM) and high-resolution TEM (HRTEM). As shown in Figure 1a–c, the In_2S_3 presented spherical-like morphology. The 3D sphere was further composed of many crisscross nanosheets. Clearly, the as-prepared In_2S_3 possessed a 2D-3D hierarchical structure. Compared to the pervious reported 2D In_2S_3 nanosheets [49] and 0D In_2S_3 nanocrystal [48], the 2D-3D In_2S_3 can facilitate light harvesting via multi-layer reflection. It also has advantages with respect to the previous method of 2D-3D In_2S_3 preparation [50], in which an amino acid (aspartic acid, serine or glycine) was necessary for assisting formation of 2D-3D hierarchical structure. Notably, the 2D-3D nanosheet-sphere structure of In_2S_3 was kept after loading Pt (Figure 1d–f). The Pt nanoparticles were not observed on the SEM image, which may have been caused by the small size of Pt. The micro-structures of In_2S_3 and Pt/In_2S_3 were further investigated by TEM and HRTEM images. As displayed in Figure 2a,b, the nanosheet-sphere structure of 2D-3D In_2S_3 can be clearly observed and the nanosheets of In_2S_3 were uniform and homogeneous. Moreover, the unambiguous lattice fringes with the d-spacing value of 0.62 nm correspond to the (111) crystal plane of cubic In_2S_3 (Figure 2c,d). After Pt photo-deposited on In_2S_3, the morphology of Pt/In_2S_3 was very similar to that of In_2S_3 (Figure 2e). In addition, small and distinguishable Pt clusters with a mean size of about 0.8 nm were observed on the nanosheets of In_2S_3 (Figure 2f). The d-spacing value of the distinct lattice fringes was also 0.62 nm, which was assigned to the (111) crystal plane of cubic In_2S_3 (Figure 2g,h). The energy-dispersive X-ray spectrometer (EDX) results indicate that Pt/In_2S_3 was composed of Pt, In and S elements, and Pt was uniformly dispersed on the In_2S_3 (Figure 2i,j).

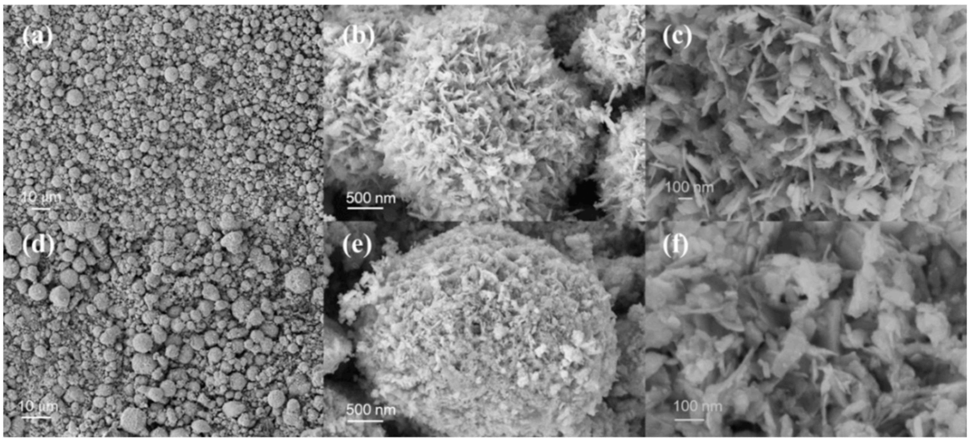

Figure 1. SEM images of (**a**–**c**) In_2S_3 and (**d**–**f**) Pt/In_2S_3.

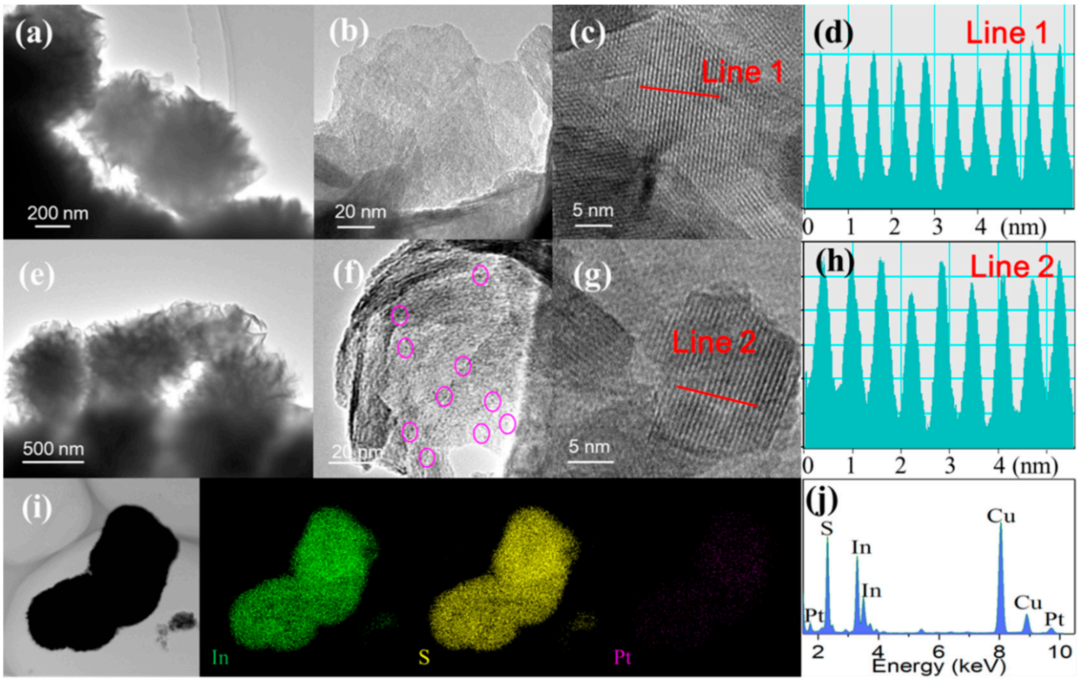

Figure 2. (**a**,**b**) TEM, (**c**) HRTEM and (**d**) corresponding FFT images of In_2S_3. (**e**,**f**) TEM and (**g**) HRTEM and (**h**) corresponding FFT images of Pt/In_2S_3 (the Pt clusters are shown in the purple circles). (**i**) EDX-mapping images and (**j**) EDX spectrum of Pt/In_2S_3.

The crystal phase, chemical composition and state were studied by powder X-ray diffraction (PXRD) and X-ray photoelectron spectroscopy (XPS). The Pt/In_2S_3 hybrid exhibited the similar PXRD pattern to the pristine In_2S_3 (Figure 3a), and the diffraction peaks of In_2S_3 and Pt/In_2S_3 both can be indexed to cubic β-In_2S_3 with Fd-3m(227) space group (JCPDS No. 65-0459). No Pt diffraction peaks were observed in the PXRD pattern of Pt/In_2S_3. It was expected because of the cluster state of Pt, i.e., due to the dispersion and low content of Pt. The ICP-OES indicated that the practical weight ratio of Pt in 1% Pt/In_2S_3 was about 0.7%. The PXRD peaks located at about 14.2, 23.3, 27.4, 28.7, 33.2, 36.3, 41.0, 43.6, 47.7, 50.0, 55.9, 56.6, 59.3, 66.6, 69.7, 77.1 and 79.5° were attributed to the diffraction of the (111), (220), (311), (222), (400), (331), (422), (511), (440), (531), (533), (622), (444), (731), (800), (662) and (840) crystal planes of cubic β-In_2S_3 (JCPDS No. 65-0459, a = b = c = 10.77 Å), respectively. The PXRD results were consistent with the above HRTEM analysis (Figure 2c,g). In the light of the above results, it can be seen that the 2D-3D morphology and crystal phase of In_2S_3 did not change after the deposition of Pt clusters. These results also indicate the stability of Pt/In_2S_3 because Pt/In_2S_3 was obtained in the PHP process of In_2S_3 by reducing $[PtCl_6]^{2-}$. Figure 3b–d presents the high-resolution XPS spectra of In 3d, S 2p and Pt 4f, respectively. For the pure In_2S_3, two peaks of In 3d observed at 445.2 and 452.7 eV were attributed to In 3d5/2 and In 3d3/2 (Figure 3b), and two peaks of S 2p located at 161.9 and 163.1 eV belonged to S 2p3/2 and S 2p1/2 (Figure 3c), respectively.

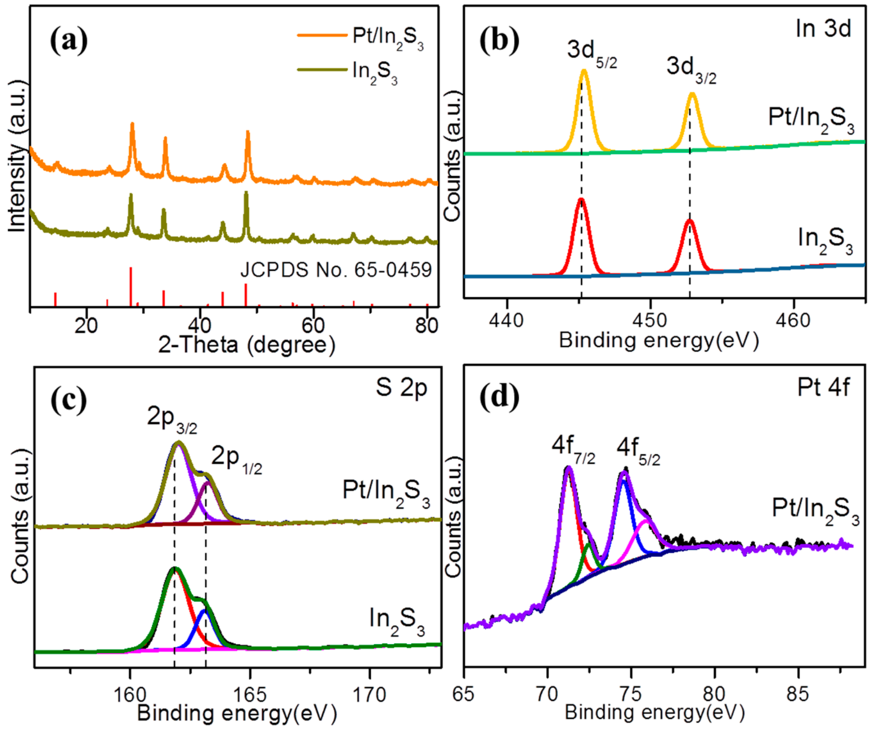

Figure 3. (**a**) XRD patterns of In_2S_3 and Pt/In_2S_3. XPS spectra of (**b**) In 3d, (**c**) S 2p and (**d**) Pt 4f.

Moreover, the spin-orbit separations of In 3d and S 2p were 7.5 and 1.2 eV, respectively. These results demonstrate that the chemical states of In and S in the as-prepared In_2S_3 were In^{3+} and S^{2-}. For the Pt/In_2S_3 hybrid, the XPS peaks of In 3d and S2p were similar to that of the pure In_2S_3. The Pt 4f exhibited two group peaks at 71.9 and 72.1 eV ($4f_{7/2}$), which corresponded to the Pt^0 and Pt^{2+}, respectively (Figure 3d). Of note, the binding energies of In 3d and S 2p of the Pt/In_2S_3 hybrid were shifted to high energy (0.1–0.2 eV) with respect to the pure In_2S_3. It was demonstrated that the binding energy shift was derived from the electronic interaction between two contacted nanomaterials, and the positive and negative shifts mean electrons were lost and gathered, respectively [31,56,57]. Thus, the strong metal-support interactions (SMSI) occurred in the Pt/In_2S_3 hybrid. Specifically, after Pt photo-deposited on In_2S_3, the majority carriers (electrons for n-type semiconductors) of In_2S_3 were migrated into Pt, and the Pt was electron enriched. The strong metal-support interactions could result in photoexcited charge separation and H_2 evolution conveniently. This is discussed further below.

The Brunauer–Emmett–Teller (BET) surface areas, optical properties and band-energy positions of In_2S_3 and Pt/In_2S_3 were studied by the nitrogen adsorption–desorption method, UV-vis diffuse reflectance spectroscopy (UV-vis DRS) and Mott–Schottky (M-S) measurements. Both In_2S_3 and Pt/In_2S_3 presented type-IV isotherms with an H3 hysteresis loop (Figure 4a). This meant that the presence of porous structures resulted from the 2D-3D In_2S_3 hierarchical structure. Correspondingly, the average pore diameters of In_2S_3 and Pt/In_2S_3 were about 13.91 and 13.64 nm, respectively. The BJH cumulative volume of pores of In_2S_3 and Pt/In_2S_3 were approximately 0.41 and 0.30 $cm^3\ g^{-1}$, respectively. The BET surface areas of In_2S_3 and Pt/In_2S_3 were approximately 63.1 $\pm$ 2.1 and 63.3 $\pm$ 2.9 $m^2\ g^{-1}$, respectively. Evidently, after Pt clusters were loaded on 2D-3D In_2S_3, the surface area change was negligible, while the pore volume and pore diameter were decreased. It is normal to observe these results because the 2D-3D In_2S_3 hierarchical structure was not altered when Pt clusters were loaded on the surfaces of In_2S_3 nanosheets. The UV-vis DRS spectra indicate that both In_2S_3 and Pt/In_2S_3 possessed well visible light absorption below 600 nm (Figure 4b). Based on DRS spectra, the band-gap energy (E_g) was determined by the Kubelka–Munk function: $(\alpha h\nu)^2 = A(h\nu - E_g)$, where A, h, α, and ν are proportionality constant, Planck constant, absorption coefficient and frequency, respectively [33,58]. Compared to the pure In_2S_3, the light absorption of Pt/In_2S_3 diminished (Figure 4b), while the E_g of Pt/In_2S_3 showed no noticeable change (both about 2.1 eV, Figure 4c). Moreover, the positive slops of M-S plots were observed on both In_2S_3 (Figure 4d) and Pt/In_2S_3 (Figure 4e), indicating that the n-type property of In_2S_3 semiconductor had not changed after Pt deposition. Interestingly, the flat potential of In_2S_3 was negatively shifted from −0.25 to −0.51 V (vs NHE) after Pt deposition. Generally, for n-type semiconductors, the flat potential lies beneath the conduction band (CB) at about −0.1 eV [56]. Therefore, the CB of In_2S_3 and Pt/In_2S_3 was located at −0.35 and −0.61 eV, respectively. According to the function: $E_g = E_{VB} - E_{CB}$ (E_{VB} and E_{CB} were the valence band energy and the CB energy, respectively), the valence band (VB) of In_2S_3 and Pt/In_2S_3 lies at 1.75 and 1.49 eV, respectively. Evidently, with respect to the pure In_2S_3 (Figure 4f), VB and CB of Pt/In_2S_3 were uplifted by 0.26 and 0.26 eV, respectively, demonstrating that the photoexcited holes showed faster mobility, thus facilitating PHP reaction [31,59]. The strong metal–support interactions between Pt and In_2S_3 resulted in electron migration from In_2S_3 into Pt. Thus, the energy bands of In_2S_3 swept upward when In_2S_3 was contacted with Pt.

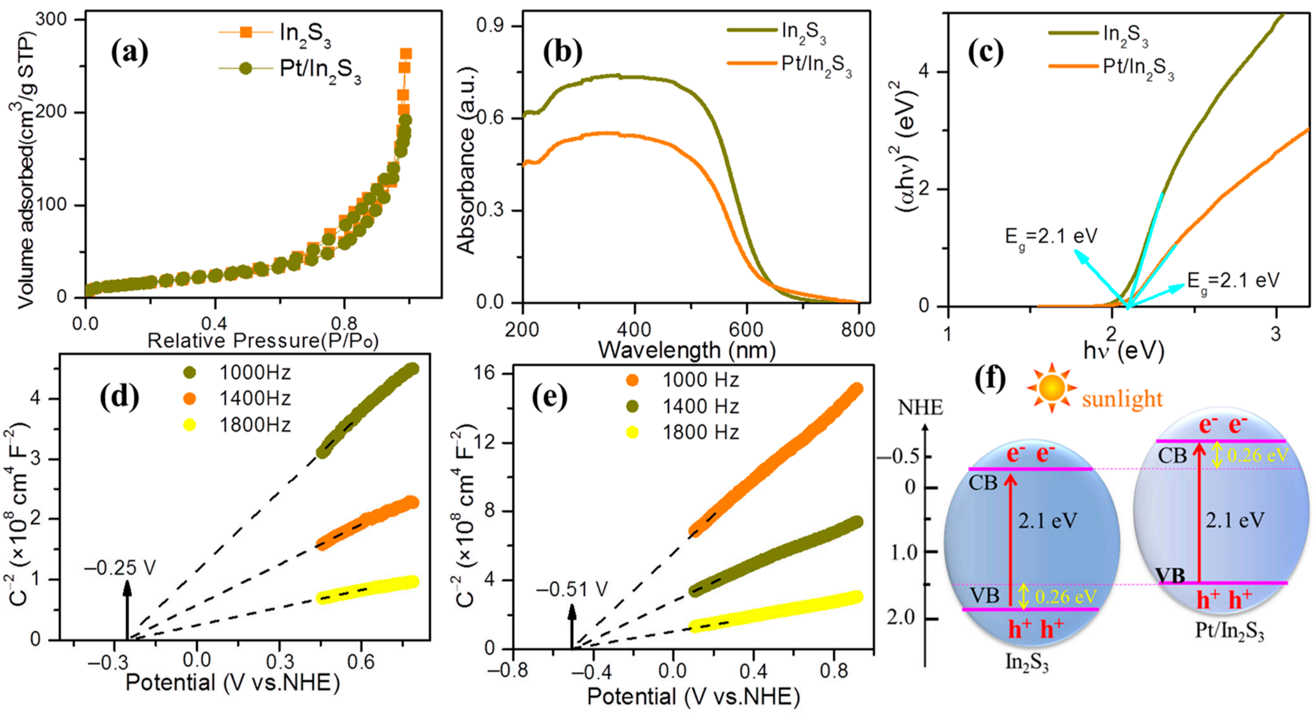

Figure 4. (**a**) Nitrogen adsorption–desorption isotherms, (**b**) UV-vis DRS spectra and (**c**) band-gap energies of In_2S_3 and Pt/In_2S_3. M-S plots of (**d**) In_2S_3 and (**e**) Pt/In_2S_3. (**f**) The relationships of band energy positions between In_2S_3 and Pt/In_2S_3.

To gain more insights into the charge carrier transportation between Pt and In_2S_3 over the Pt/In_2S_3 hybrid, the work function of In_2S_3 was measured by an ultraviolet photoelectron spectroscopy (UPS), As presented in Figure 5a, the work function of In_2S_3 was 4.66 eV (21.22 − (16.77 − 0.21) = 4.66). It was smaller than the work function of Pt (5.65 eV) [14]. Moreover, the carrier densities (N_D) of In_2S_3 and Pt-modified In_2S_3 (Pt/In_2S_3) were detected from M-S plots via the function: $N_D = (2/e\varepsilon\varepsilon_0)[dU_{FL}/d(1/C^2)] = (2/e\varepsilon\varepsilon_0)(1/k_{M\text{-}S})$. Here, e, ε_0, ε, $k_{M\text{-}S}$, U_{FL} and C are elementary charge, vacuum permittivity, relative permittivity (8.4 for In_2S_3 [23]), the slope of the M-S curve, Fermi level potential and capacitance, respectively. Evidently, after Pt deposition on In_2S_3, the carrier density of In_2S_3 was always reduced under different frequencies (Figure 5b). Based on the results of work function and carrier density, the metal–support interactions and consequential electron transportation between Pt and In_2S_3 are illustrated in Figure 5c–e. The In_2S_3

possessed a higher Fermi level ($E_F = E_{vac} - W_F$, where W_F, E_{vac} and E_F are work function, vacuum level and Fermi level, respectively) than Pt (Figure 5c). Thus, the electrons were transported from In_2S_3 into Pt, which resulted in a N_D decrease in In_2S_3 and the formation of the Schottky junction (Figure 5d). The Schottky barrier with height of 0.99 eV would facilitate photoexcited electrons transportation from In_2S_3 into Pt and inhibit the backflow of electrons from Pt into In_2S_3 again (the barrier height is the difference of Fermi levels of In_2S_3 and Pt ($-4.66 - (-5.65) = 0.99$)). Simultaneously, the photoexcited holes left at In_2S_3 (Figure 5e). Consequently, the photoexcited electron-hole pairs of In_2S_3 were separated spatially through Pt/In_2S_3 Schottky junctions. In the light of the above analyses, the Pt/In_2S_3 hybrid may be fit for PHP.

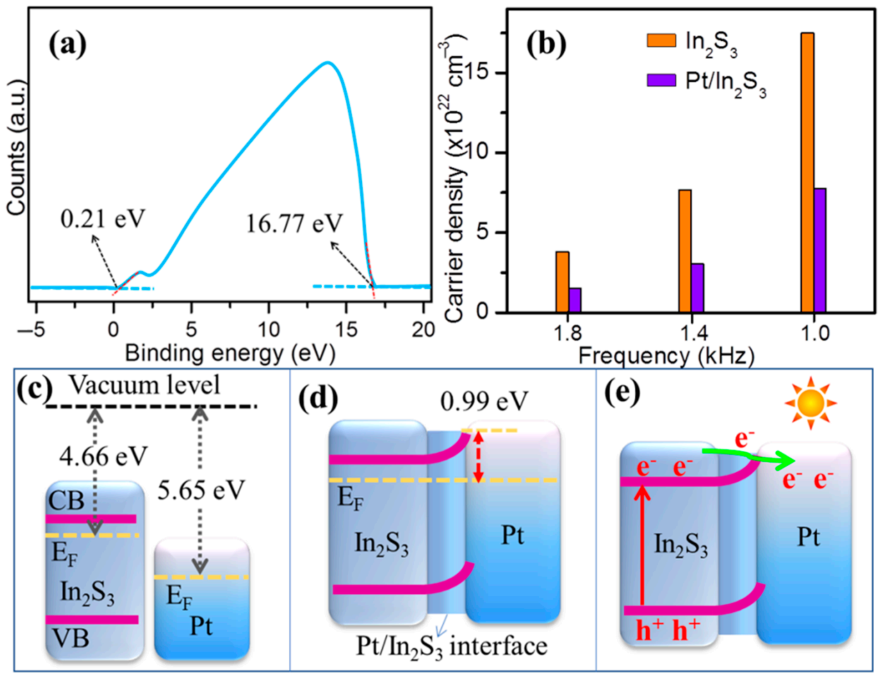

Figure 5. (**a**) UPS spectrum of In_2S_3. (**b**) Carrier densities of In_2S_3 before and after Pt modification. Energy level diagrams for In_2S_3 and Pt (**c**) before and (**d**) after interfacing. (**e**) Illustration of photoexcited electrons transfers from In_2S_3 into Pt over Pt/In_2S_3 interface under light irradiation.

2.2. Evalution of PHP Activity

The PHP activity was evaluated by photocatalytic selective oxidation of phenylcarbinol ($PhCH_2OH$) under simulated sunlight. The two control groups (with photocatalyst in the dark and without photocatalyst under light irradiation) were firstly performed and showed no H_2 production. Then, we detected PHP activities of In_2S_3 and Pt/In_2S_3 composites with different content of Pt (0.1%, 0.3%, 0.5% and 1%). As depicted in Figure 6a, the pure In_2S_3 exhibited low PHP activity (H_2: 0.9 mmol g^{-1} h^{-1}). However, the PHP activity of the In_2S_3 was significantly enhanced by loading a low amount of Pt. The photocatalytic H_2 evolution rates of 0.1%, 0.3%, 0.5% and 1% Pt/In_2S_3 hybrids were about 4.1, 22.1, 17.1 and 14.6 mmol g^{-1} h^{-1}, respectively. The PHP activities of these Pt/In_2S_3 hybrids appeared to have a volcano-like distribution. The 0.3% Pt/In_2S_3 hybrid exhibited the highest PHP activity, which was approximately 24.56 times that of the pure In_2S_3. It indicates that the apparent PHP kinetics of In_2S_3 was meaningfully improved by loading Pt clusters. The as-synthesized Pt/In_2S_3 also exhibited a higher H_2 production rate (7.97 mmol g^{-1} h^{-1}) under visible light irradiation than the reported $Pt/Zn_3In_2S_6$ [14], Pt/CdS [42], etc [21–24]. (Table 1). Moreover, negligible PHP activity was detected for pure water splitting over 0.3% Pt/In_2S_3 because of the sluggish oxidation half-reaction and significant Gibbs free energy change ($H_2O = H_2 + 1/2O_2$, $\Delta G \approx 238$ kJ mol^{-1} >> 0). Compared to PHP through overall water splitting, the thermodynamics of PHP was also remarkably ameliorated ($PhCH_2OH$

= PhCHO + H_2, $\Delta G \approx 28$ kJ mol^{-1}). It should also be noted that the oxidized products of phenylcarbinol over the 0.3% Pt/In_2S_3 hybrid were almost entirely benzaldehyde (the selectivity was nearly 100%). It may have been caused by the suitable oxidative potential of Pt/In_2S_3 for selectively oxidizing $PhCH_2OH$ into PhCHO. Evidently, in the dual-function photoredox reaction system, Pt/In_2S_3 not only can selectively oxidize phenylcarbinol into fine value-added chemicals (benzaldehyde) with high selectivity but also can obtain clean energy (H_2) simultaneously. Moreover, the turnover number (TON) based on the amount of Pt was calculated to be about 9576 after 4 h. Notably, the corresponding turnover frequency (TOF) was about 2394 h^{-1}, which is comparable with the traditional thermal catalytic system (1109 h^{-1}) [27,60].

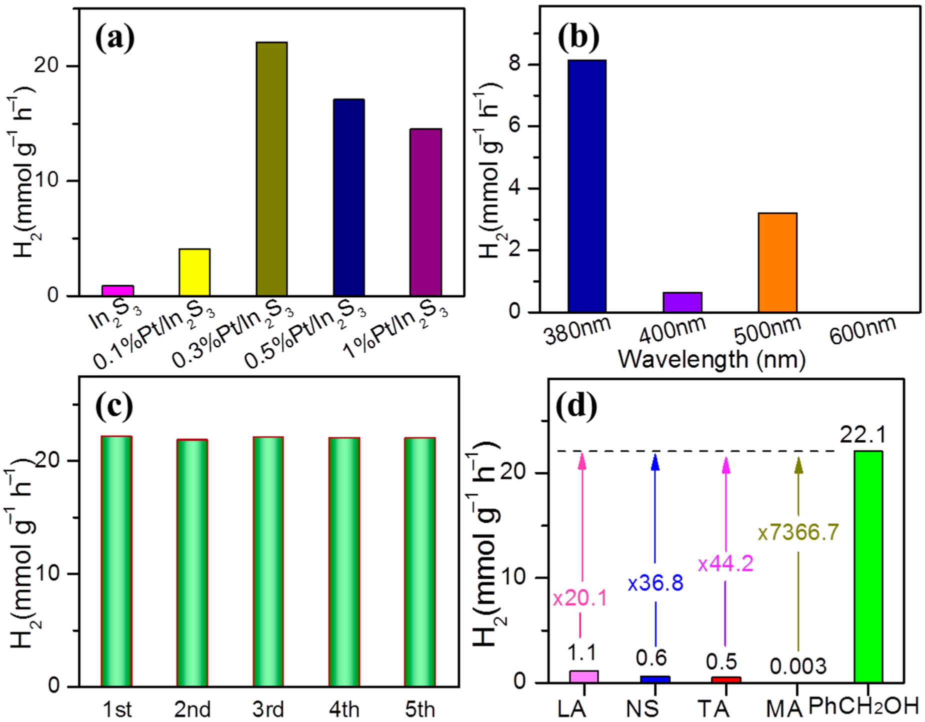

Figure 6. (**a**) The PHP activity of In_2S_3 and Pt/In_2S_3 with different Pt weight ratios for photocatalytic selective oxidation of phenylcarbinol and H_2 production under simulated sunlight irradiation. (**b**) The PHP activity of 0.3% Pt/In_2S_3 under monochromatic light irradiation with different wavelengths. (**c**) The PHP activity of 0.3% Pt/In_2S_3 under simulated sunlight irradiation for 5 recycles. (**d**) Comparison of 0.3% Pt/In_2S_3 PHP activity in different reaction systems (LA, NS, TA, MA and $PhCH_2OH$ presents aqueous solutions of lactic acid, Na_2S, triethanolamine, methanol and phenylcarbinol, respectively) under simulated sunlight irradiation.

Table 1. Comparison of photocatalytic performance over different photocatalysts for photocatalytic H_2 production.

Photocatalyst	Light Source	Reagents	H_2 Evolution (mmol g^{-1} h^{-1})	Ref.
Pt/In_2S_3	$\lambda \geq 420$ nm	$PhCH_2OH$	7.97	This Work
Pt/CdS	$\lambda > 420$ nm	$PhCH_2OH$	4.9	[42]
Pt/$Zn_3In_2S_6$	$\lambda \geq 420$ nm	$PhCH_2OH$	0.9	[14]
Pt/g-C_3N_4	$\lambda > 420$ nm	TEOA	3.02	[21]
MoP/In_2S_3	$\lambda \geq 420$ nm	Lactic acid	0.5	[22]
$Zn_3In_2S_6In_2S_3$	$\lambda > 400$ nm	bisphenol A	0.08	[23]
PdS/In_2S_3	$\lambda > 420$ nm	Na_2S/Na_2SO_3	3.6	[24]

Figure 6b shows the PHP activity of 0.3% Pt/In_2S_3 under monochromatic light with different wavelengths. The 380 nm-light and 500 nm-light driven PHP activities were higher than 400 nm. It indicates that the PHP activity of Pt/In_2S_3 was not only dependent on its light absorption spectrum. It is comprehensible because the PHP activity was an overall effect of light absorption, incident light intensity and light energy. Pt/In_2S_3 was inactive under 600 nm light because it was longer than the excitation wavelength of In_2S_3 (<590 nm). Nevertheless, the PHP activity of Pt/In_2S_3 under 500 nm light could still reach up to 3.2 mmol g^{-1} h^{-1} with 3.72% of apparent quantum efficiency. In addition, the 0.3% Pt/In_2S_3 hybrid demonstrated good photocatalytic stability with little H_2 production decrease (<0.5%) after five recycles (Figure 6c). To compare this dual-function photoredox reaction system with the sacrificial agent PHP, the classic sacrificial agents: lactic acid (LA), Na_2S (NS), triethanolamine (TA) and methanol (MA) were chosen [20]. Figure 6d depicts PHP comparisons between sacrificial agents and $PhCH_2OH$ over 0.3% Pt/In_2S_3 under the same reaction conditions. Specifically, the PHP rates of 0.3% Pt/In_2S_3 only reached 1.1, 0.6, 0.5 and 0.003 mmol g^{-1} h^{-1} when LA, NS, TA and MA were added into the reaction system, respectively. Clearly, the superior PHP rate of 0.3% Pt/In_2S_3 was achieved through using phenylcarbinol, which was about 20.1, 36.8, 44.2 and 7366.7 times higher than that using LA, Na_2S and TEOA, respectively. These results confirm the superiority of photocatalytic selective conversion organics coupled with photocatalytic H_2 production, in which organics were selectively transformed into high value-added chemicals and simultaneous H_2 with the enhanced production rate that could be obtained.

2.3. Photocatalytic Mechanism

The photocatalytic activity demonstrated that it was mainly influenced by three factors: light absorption, active sites (likely surface area) and photoexcited charges separation and transportation [61–63]. Specifically, the photocatalysts are excited by the incident light to produce electron-hole pairs, which are then separated and transferred onto the active sites for redox reactions. Based on the above characterizations, after Pt clusters deposition on the 2D-3D In_2S_3, the light absorption did not become stronger (Figure 4b), and the surface area underwent a negligible change (Figure 4a). The surface area was not the main factor for the enhanced PHP activity, which is consistent with the reported Pt-loaded photocatalysts [64,65]. Therefore, light absorption and surface area are not the main factors for the boosted PHP activity. However, the electron circulating and the uplifted energy bands were observed on Pt/In_2S_3 hybrid as the result of the strong metal–support interactions between In_2S_3 and Pt. To understand the reasons behind the enhanced photocatalytic activity, the photoexcited charge behaviors were investigated. As shown in Figure 7a, the photocurrent of the Pt/In_2S_3 improved 2.08 times in contrast to the pure In_2S_3 under simulated sunlight illumination, suggesting efficient charge separation and transfer [66,67]. In addition, the photocurrent of the Pt/In_2S_3 still increased 1.85 times when $MVCl_2$ was added into the bath solution as an electron scavenger (Figure 7b). Moreover, the charge transport efficiency (η_{tra}) can be evaluated by the function: $\eta_{tra} = J_{H2O}/J_{MVCl2}$ (J_{H2O} and J_{MVCl2} are the photocurrent densities of the sample with and without $MVCl_2$, respectively) [68–70]. As expected, 90.1% of the charge transport efficiency could be achieved over the Pt/In_2S_3 hybrid, which was approximately 1.13 times of the pure In_2S_3. These results indicate that the separation and transportation of In_2S_3 can be improved by loading Pt clusters. To further evaluate the impact of strong metal–support interactions on charge separation and transportation, the electrochemical impedance spectroscopy (EIS) [71] and linear sweep voltammetry (LSV) tests were carried out [5,14]. Pt/In_2S_3 exhibited a smaller arc radius than In_2S_3 (Figure 7c), and the charge transport resistance of Pt/In_2S_3 (30.5 Ω) was weaker than that of In_2S_3 (33.9 Ω). This means that the loaded Pt clusters can speed charge separation and transportation of In_2S_3. This result is in line with the photocurrent analysis and can be further confirmed by LSV curves. As displayed in Figure 7d, compared to the pure In_2S_3, the current density of Pt/In_2S_3 exhibited a visible enhancement under light irradiation. In addition, the H_2 evolution overpotential of Pt/In_2S_3 (−0.64 V) was 0.34 V lower than that of In_2S_3 (−0.98 V), which is conducive to H_2 evolution. Consequently, it can be concluded that the improved charge separation-transportation and the reduced H_2 evolution overpotential contribute to the efficient PHP activity of Pt/In_2S_3.

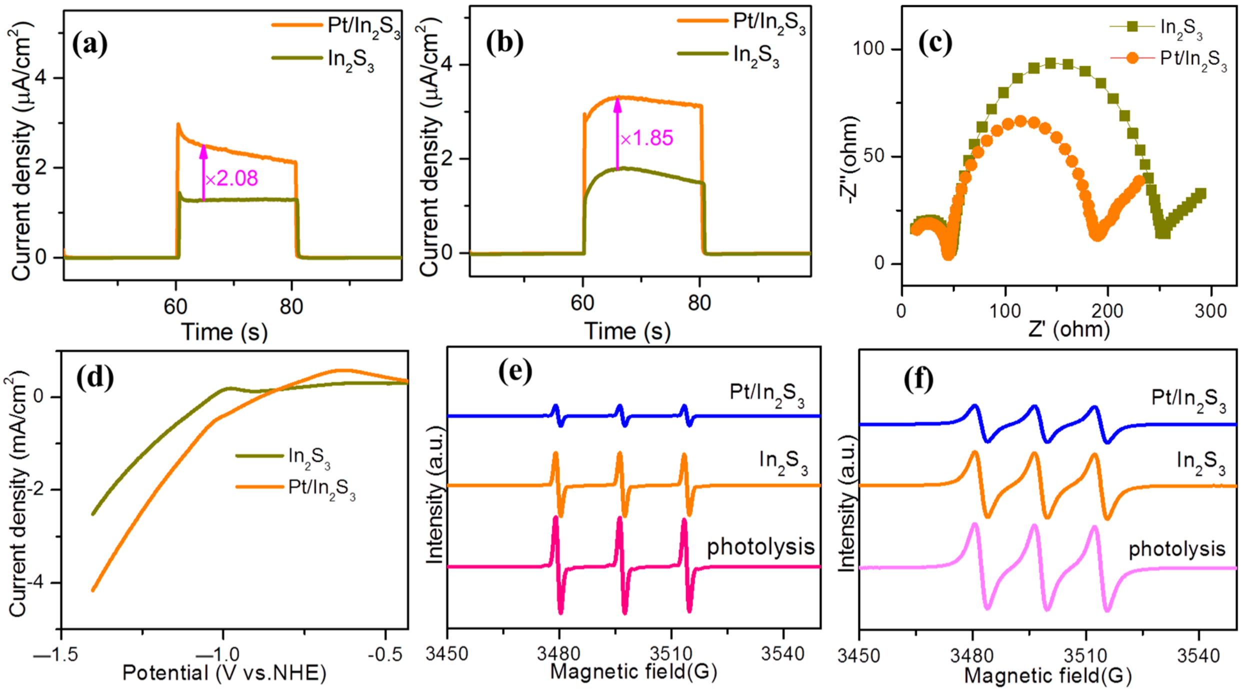

Figure 7. Transient photocurrent responses of catalysts (**a**) without and (**b**) with methyl viologen dichloride ($MVCl_2$). (**c**) EIS plots, (**d**) LSV curves, (**e**) TEMPO-e^- EPR spectra and (**f**) TEMPO-h^+ EPR spectra of In_2S_3 and Pt/In_2S_3.

To understand the in-depth information behind these results, the utilization rates of photoexcited electrons (e^-) and holes (h^+) were studied through in situ electron paramagnetic resonance (EPR) measurements [68]. As the control group, photolysis refers to the reaction system without photocatalysts (Figure 7e,f). In other words, the signal of photolysis is the intrinsic signal of the active TEMPO. The EPR signal intensity is reduced when TEMPO is captured by photoexcited electrons or holes [68]. When In_2S_3 or Pt/In_2S_3 was added into the reaction system, the EPR signals were both reduced for detecting electrons (Figure 7e) and holes (Figure 7f). This indicates that the photoexcited electrons and holes can be separated and transported on the surfaces of In_2S_3 and Pt/In_2S_3. Notably, the EPR signal of Pt/In_2S_3 for photoexcited electrons was significantly lower than that of In_2S_3 (Figure 7e). This suggests efficient electron separation and transportation from In_2S_3 to Pt for reducing water/protons to H_2. In addition, the weaker EPR signal of TEMPO on Pt/In_2S_3 was also observed than that on In_2S_3 in the presence of $PhCH_2OH$ under simulated sunlight illumination (Figure 7f). This indicates efficient hole transportation from the In_2S_3 component of Pt/In_2S_3 to reactive molecules of $PhCH_2OH$. Thus, the efficient separation and transportation of the photogenerated holes and electrons contribute to the enhanced PHP activity of the Pt/In_2S_3 hybrid. The photoexcited holes can be fleetly consumed by $PhCH_2OH$ to produce PhCHO. Simultaneously, the photoexcited electrons were spent by H^+/H_2O to produce H_2.

To further inspect the conversion process of $PhCH_2OH$ in this dual-function photocatalysis system, the in situ EPR with the addition of DMPO and in situ DRIFT were carried out [5,31,72–74]. As presented in Figure 8a, $PhCH_2OH$ with DMPO under light irradiation could not produce EPR signals (photolysis). However, sextet peaks belonging to carbon-centered radicals (.CH(OH)Ph) [5,68] were observed on In_2S_3 and Pt/In_2S_3. This means that the conversion process of $PhCH_2OH$ is a free radical reaction. Moreover, the EPR intensity of Pt/In_2S_3 was more intense than In_2S_3, implying efficient charge separation-transportation and fast $PhCH_2OH$ dehydrogenation on Pt/In_2S_3. In addition, one peak at 1703 cm^{-1} ($\nu_{C=O}$) fell to the carbonyl group (C=O) of benzaldehyde (PhCHO) and doublet peaks at 2873 and 2935 cm^{-1} ($\nu_{C\text{-}H}$), attributed to the carbon–hydrogen bond (C-H) of the aldehyde group, were clearly observed on Pt/In_2S_3 under simulated sunlight (Figure 8b). These results indicate that $PhCH_2OH$ is selectively oxidized into PhCHO via a carbon-centered radical process. The effects of the reactive species on PHP were also investigated by the trapping experiments (Figure 8c). Triethanolamine (TA) and carbon tetrachloride (CTC) were used as trapping agents for photoexcited holes and electrons, respectively. When TA was added into the reaction system, the H_2 production rate decreased. This indicates that the dehydrogenation of $PhCH_2OH$ to H_2 production is restrained by TA. For the trapping agent CCl_4, a relatively large decrease was observed in the H_2 production rate. This indicates that the photogenerated electrons are major reductive species for the reduction in protons to H_2. These results suggest that synergistic effect occurred between $PhCH_2OH$ dehydrogenation and H_2 production.

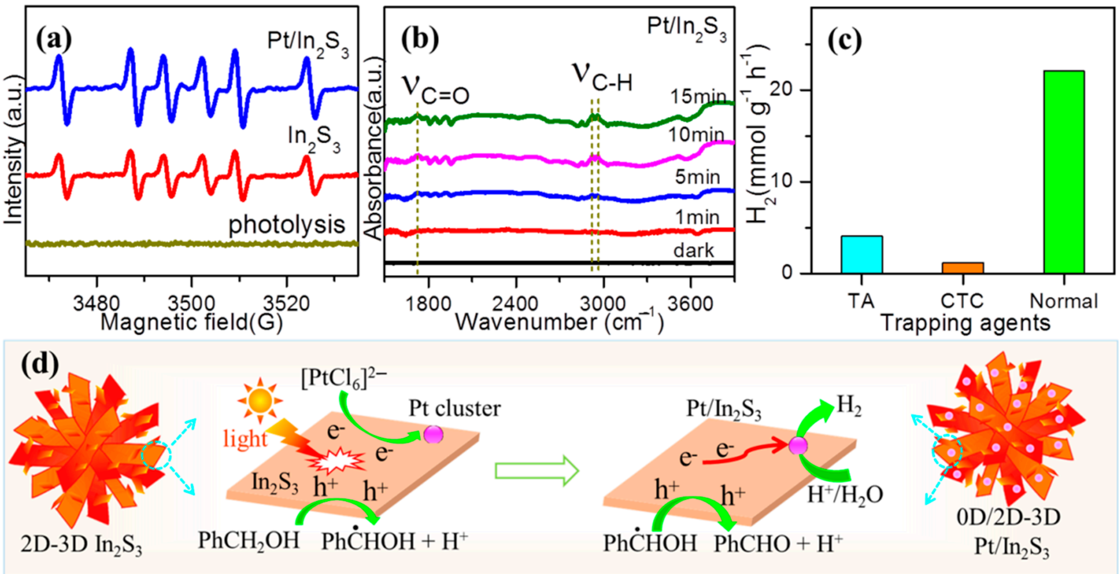

Figure 8. (**a**) EPR spectra of DMPO-CH(OH)Ph over different photocatalysts. (**b**) In situ DRIFTS spectra of the 0.3% Pt/In_2S_3 hybrid with the existence of $PhCH_2OH$ under simulated sunlight. (**c**) The effect of the trapping agents on the PHP over the 0.3% Pt/In_2S_3 hybrid. (**d**) Illustration of the formation and photocatalytic mechanism of the 0D/2D-3D Pt/In_2S_3 heterostructure.

From the above analysis, the photocatalytic mechanism was proposed as depicted in Figure 8c. Under simulated sunlight irradiation, the photoexcited electrons and holes were generated on the In_2S_3 nanosheets. Then, on the one hand, $PhCH_2OH$ was oxidized into .CH(OH)Ph, and the .CH(OH)Ph free radical was further oxidized into PhCHO by the photoexcited holes located at In_2S_3. On the other hand, the photoexcited electrons were first consumed by $[PtCl_6]^{2-}$ to produce Pt clusters and were then separated and transported from In_2S_3 into Pt clusters efficiently to produce H_2 by reducing H^+/H_2O. During this redox process, $[PtCl_6]^{2-}$ was reduced by the photoexcited electrons on the surfaces of In_2S_3, and Pt^0 was anchored at the separated electron location. Thus, the as-synthesized Pt/In_2S_3 heterostructure would facilitate the electron transportation from In_2S_3 into Pt and improve PHP activity. Due to the competing reactions of H_2 evolution, the Pt cluster was in the optimized state for H_2 production. During the coupled redox reaction of $PhCH_2OH$ oxidation and H_2 evolution, one molecule of $PhCH_2OH$ was oxidized into one molecule of PhCHO by consuming two photoexcited holes. Simultaneously, one molecule of H_2 was produced by expending two electrons. Thus, the efficient, stable and atom-economic dual-function photocatalytic reaction system was achieved on the 0D/2D-3D Pt/In_2S_3 heterostructures.

3. Experiments and Methods

3.1. Materials

5,5-dimethyl-1-pyrroline-N-oxide (DMPO) and 2,2,6,6-Tetramethylpiperidin-1-oxyl (TEMPO) for EPR-spectroscopy were purchased from Sigma-Aldrich. Indium chloride tetrahydrate ($InCl_3 \cdot 4H_2O$, 99.9%), thioacetamide (C_2H_5NS, ≥99.0%), chloroplatinic acid hexahydrate ($H_2PtCl_6 \cdot 6H_2O$, Pt ≥35.7%), potassium ferrocyanide trihydrate ($K_4[Fe(CN)_6] \cdot 3H_2O$, ≥99.5%), phenylcarbinol (C_7H_8O, ≥99.0%), lactic acid ($C_3H_6O_3$, 85%), triethanolamine ($C_6H_{15}NO_3$, ≥99.0%), sodium sulfate (Na_2SO_4, ≥98%), potassium chloride (KCl, 99.8%), potassium ferricyanide ($K_3[Fe(CN)_6]$, 99%) and other used reagents were all analytical reagents and were used directly with no further purification.

3.2. Preparation of 2D-3D In_2S_3 and 0D/2D-3D Pt/In_2S_3

The 0D/2D-3D Pt/In_2S_3 heterostructure was prepared as depicted in Figure 9. Briefly, $InCl_3$ was wholly dissolved into acid solution and reacted with thioacetamide (TAA) to form $[In(TAA)_4]^{3+}$ and $[In(TAA)_6]^{3+}$ complexes via In-S bonds [75]. Then, these complexes underwent the hydrothermal process to produce 2D-3D In_2S_3. In_2S_3 was easily formed because the solubility product constant (Ksp) of In_2S_3 was very small (5.7×10^{-74}) [75]. Finally, Pt/In_2S_3 heterostructure was obtained by an in situ photodeposition process. Namely, the Pt/In_2S_3 was synthesized in the process of PHP coupled with simultaneously selective phenylcarbinol conversion.

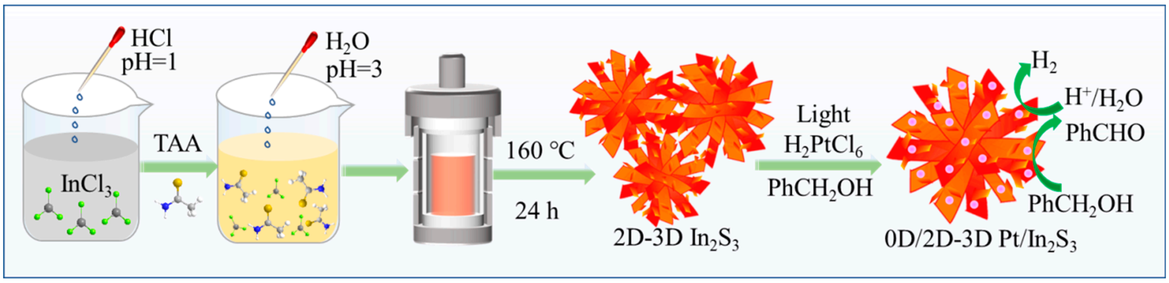

Figure 9. The preparation procedure of the 0D/2D-3D Pt/In_2S_3 heterostructure.

In a typical synthesis, 1 mmol $InCl_3 \cdot 4H_2O$ was dissolved in deionized water, and the pH of the $InCl_3$ solution was adjusted to 1.0 by adding HCl to prevent $InCl_3$ hydrolysis. Then, 2.5 mmol C_2H_5NS was gradually added into the above solution and constantly stirred. The pH of the above solution was adjusted to 3.0 again by adding H_2O. The above solution was transferred to a 100 mL Teflon-lined stainless-steel reactor and held at 180 °C for 24 h. After natural cooling to 25 °C, the orange precipitate was collected and washed with distilled water and anhydrous ethanol several times. Finally, the sediments were dried in a vacuum oven at 60 °C for 2 h. The pure 2D-3D In_2S_3 was obtained. The 0D/2D-3D Pt/In_2S_3 heterostructure was obtained by an in situ photodeposition method in the process of photocatalytic selective conversion of phenylcarbinol into benzaldehyde and H_2. The details are presented in the following section.

3.3. Photocatalytic Activity Test

The photocatalytic H_2 generation was carried out in a gas-tight Pyrex reactor. The 300 W Xenon lamp (PLS-SXE300D, Perfect Light Co., Beijing, China) was used as the simulated solar light. Typically, 10 mg In_2S_3 powders were dispersed in 10 mL phenylcarbinol solution and then different amounts of $H_2PtCl_6 \cdot 6H_2O$ were added. After bubbling argon to remove dissolved oxygen, the suspension was irradiated for photocatalytic H_2 production. After irradiation for 2 h, the H_2 was quantified using a gas chromatograph spectrometer

(GC 9790II, Fuli, Wenling, China) equipped with a molecular sieve 5A column. The reaction liquor was detected by high performance liquid chromatography (HP-LC, watersE2695, MA, USA). The detector of the HP-LC was PDA 2998. The mobile phase consisted of 40% deionized water and 60% acetonitrile with a flow rate of 1 mL min^{-1}. Finally, the precipitate ($Pt//In_2S_3$) after light exposure was collected, washed with ethanol and dried at 60 °C for 2 h. Catalysts with different Pt content added were rewritten as x% Pt/In_2S_3 (x is a weight ratio of Pt in the Pt/In_2S_3 composite, x = 0.1, 0.3, 0.5, 1.0). For comparison, the pure In_2S_3 was also quantitatively analyzed for H_2 production without adding $H_2PtCl_6·6H_2O$. The apparent quantum efficiency (AQE) for H_2 evolution was obtained by the following equation: AQE = $(2 \times N_H/N_p) \times 100\%$, where N_H and N_p are the numbers of evolved H_2 molecules and incident photons, respectively. Turnover number (TON) was calculated based on the quantity of H_2 and Pt: TON = N_H/N_{pt}, where N_{pt} is the number of Pt. The turnover frequency (TOF) was measured via TON divided by reaction time. Benzaldehyde selectivity was calculated by the equation: Selectivity = $[C_{CHO}/(C_0\text{-}C_{OH}] \times 100\%$, where C_0, C_{OH} and C_{CHO} are the concentrations of phenylcarbinol, the residual phenylcarbinol and the corresponding aldehydes, respectively.

3.4. Characterization

Powder X-ray diffraction (PXRD) pattern of the sample was determined by a Bruker D8 X-ray powder diffractometer using Ni-filtered Cu Kα radiation. The microstructure and morphologies of the prepared samples were carried out by scanning electron microscope (SEM, Regulus 8200, Hitachi Limited, Tokyo, Japan) and transmission electron microscope (TEM, JEM2100, JEOL, Akishima-shi, Japan). Elemental mappings were measured using an energy-dispersive X-ray spectrometer (EDX). X-ray photoelectron spectroscopy (XPS, Thermo Scientific, Massachusetts, America) measurements were performed on Thermo Scientific ESCA Lab250 spectrometer. All the binding energies were referred to the C 1s peak at 284.6 eV of the surface adventitious carbon. UV-vis diffuse reflectance spectra (DRS) of the powders were obtained on a UV-vis spectrophotometer (Shimadzu UV-3600, Kyoto, Japan), with $BaSO_4$ used as a reference. Brunauer–Emmett–Teller (BET) surface areas were tested on a Micromeritics ASAP 2460 instrument. In situ diffuse reflectance infrared Fourier transform spectroscopy (DRIFT) measurements were detected on a Nicolet 8700 FTIR spectrometer. The carbon-centered radicals and the photoexcited charges (electrons and holes) were in situ seen on an electron paramagnetic resonance (EPR, A300, Karlsruhe, Bruker, Germany) by DMPO and TEMPO as trapping agents, respectively. The work function of the In_2S_3 was obtained on an ultraviolet photoelectron spectroscopy (UPS, Thermo ESCALAB 250XI, (Waltham, MA, USA). The actual Pt content in the Pt/In_2S_3 sample was measured by an inductively coupled plasma optical emission spectrometry (ICP-OES, Agilent 5110, Santa Clara, CA, USA).

3.5. Photoelectrochemical Property Test

The photoelectrochemical (PEC) tests were carried out on a CHI-660E electrochemical workstation (CH Instruments, Bee Cave, TX, USA). An Ag/AgCl and a Pt wire were used as the reference electrode and the counter electrode, respectively. The sample powder was deposited on the FTO (50 mm × 50 mm) as a working electrode. Typically, a uniform solution was obtained by ultrasonically dispersing 5 mg samples into 400 µL deionized water. Then, 20 µL of the above solution were deposited on the FTO substrate. The working electrode was obtained after drying at room temperature. The transient photocurrent responses, linear sweep voltammetry (LSV) plots and Mott–Schottky (M-S) plots were detected in a 0.2 M Na_2SO_4 aqueous solution. Electrochemical impedance spectroscopy (EIS) Nyquist plots were detected in 0.1 M KCl solution containing 0.1 M $K_3[Fe(CN)_6]/K_4[Fe(CN)_6]$.

4. Conclusions

In summary, a 2D-3D In_2S_3 hierarchical structure decorated by 0D Pt clusters was successfully fabricated by the sequential hydrothermal process and in situ photodeposition.

The strong metal–support interactions (SMSI) of the Pt/In_2S_3 hybrid improved the charge separation and transportation. and thus. resulted in the significant enhancement of photocatalytic H_2 production. The optimized 0.3% Pt/In_2S_3 exhibited the highest and stable photocatalytic activity with 22.1 mmol g^{-1} h^{-1} of H_2 evolution rate and almost 100% selectivity of benzaldehyde production. In addition, the turnover frequency of 0.3% Pt/In_2S_3 reached up to approximately 2394 h^{-1}, and 3.72% of apparent quantum efficiency was achieved under 500 nm light irradiation. Coupling phenylcarbinol conversion with H_2 evolution was superior to the traditional sacrificial agents. The H_2 production using phenylcarbinol was approximately 20.1, 36.8, 44.2 and 7366.7 times higher than that using lactic acid, Na_2S, triethanolamine and methanol as sacrificial agents under the same reaction condition, respectively. Notably, in this dual-function photocatalysis, the photoexcited holes located at the In_2S_3 were utilized for selective oxidizing phenylcarbinol into value-added fine chemicals benzaldehyde; conversely, the photoexcited electrons on the In_2S_3 were used firstly for reducing $[PtCl_6]^{2-}$ to fabricate Pt clusters anchored at the separated electron location and then transported from the In_2S_3 to the Pt clusters for H_2 production. The Pt clusters were stable, and the charge transport efficiency of In_2S_3 reached up to approximately 90.1% by the modification of the Pt clusters. Moreover, the synergistic effect occurred between $PhCH_2OH$ dehydrogenation and H_2 production. This work is expected to aid the design of efficient and stable photocatalysts to simultaneously utilize photoexcited holes and electrons, thereby gaining the value-added fine chemicals and clean energy in one reaction system.

Author Contributions: H.Z.: investigation, data curation, writing—original draft preparation. P.X.: formal analysis, resources, writing—original draft preparation. B.L.: resources, methodology. Q.L.: software. X.Z.: resources, formal analysis, writing—review and editing. S.Z.: resources. Z.R.: validation. S.C.: funding acquisition, formal analysis, writing—review and editing, supervision. S.M.: Conceptualization, formal analysis, writing—review and editing, supervision, project administration, funding acquisition. All authors have read and agreed to the published version of the manuscript.

Funding: This work was supported by the National Natural Science Foundation of China (NSFC, 52002142, 51972134, 52272297 and 52002142), the Foundation of Anhui Province for Distinguished Young Scholars (2022AH020038), the Foundation of Anhui Province for Outstanding Young Graduate-student Advisors (2022yjsds036), Open Project Program of the State Key Laboratory of Photocatalysis on Energy and Environment (SKLPEE-KF201804 and SKLPEE-KF202202) in Fuzhou University, the Natural Science Foundation of Anhui Province (2108085MB43), the University Natural Science Research Project of Anhui Province (KJ2021A0524).

Data Availability Statement: Data only available upon request from corresponding author.

Conflicts of Interest: The authors declared that there is no conflict of interest.

References

1. Fujishima, A.; Honda, K. Electrochemical Photocatalysis of Water at a Semiconductor Electtode. *Nature* **1972**, *238*, 37–38. [CrossRef]
2. Nishiyama, H.; Yamada, T.; Nakabayashi, M.; Maehara, Y.; Yamaguchi, M.; Kuromiya, Y.; Tokudome, H.; Akiyama, S.; Watanabe, T.; Narushima, R.; et al. Photocatalytic solar hydrogen production from water on a 100-m^2 scale. *Nature* **2021**, *598*, 304–307. [CrossRef]
3. Liu, L.; Du, S.; Guo, X.; Xiao, Y.; Yin, Z.; Yang, N.; Bao, Y.; Zhu, X.; Jin, S.; Feng, Z.; et al. Water-Stable Nickel Metal-Organic Framework Nanobelts for Cocatalyst-Free Photocatalytic Water Splitting to Produce Hydrogen. *J. Am. Chem. Soc.* **2022**, *144*, 2747–2754. [CrossRef]
4. Rasool, M.A.; Sattar, R.; Anum, A.; Al-Hussain, S.A.; Ahmad, S.; Irfan, A.; Zaki, M.E. An Insight into Carbon Nanomaterial-Based Photocatalytic Water Splitting for Green Hydrogen Production. *Catalysts* **2023**, *13*, 66. [CrossRef]
5. Meng, S.; Chen, C.; Gu, X.; Wu, H.; Meng, Q.; Zhang, J.; Lei, W. Efficient Photocatalytic H_2 Evolution, CO_2 Reduction and N_2 Fixation Coupled with Organic Synthesis by Cocatalyst and Vacancies Engineering. *Appl. Catal. B Environ.* **2021**, *285*, 119789. [CrossRef]
6. Cai, M.D.; Cao, S.Y.; Zhuo, Z.Z.; Wang, X.; Shi, K.Z.; Cheng, Q.; Xue, Z.M.; Du, X.; Shen, C.; Liu, X. Fabrication of Ni_2P Cocatalyzed CdS Nanorods with a Well-Defined Heterointerface for Enhanced Photocatalytic H_2 Evolution. *Catalysts* **2022**, *12*, 417. [CrossRef]

7. Battula, V.R.; Jaryal, A.; Kailasam, K. Visible light-driven simultaneous H_2 production by water splitting coupled with selective oxidation of HMF to DFF catalyzed by porous carbon nitride. *J. Mater. Chem. A* **2019**, *7*, 5643–5649. [CrossRef]
8. Ripple, W.J.; Wolf, C.; Newsome, T.M.; Galetti, M.; Alamgir, M.; Crist, E.; Mahmoud, M.I.; Laurance, W.F. World Scientists' Warning to Humanity: A Second Notice. *BioScience* **2017**, *67*, 1026–1028. [CrossRef]
9. Xu, D.; Zhang, S.-N.; Chen, J.-S.; Li, X.-H. Design of the Synergistic Rectifying Interfaces in Mott-Schottky Catalysts. *Chem. Rev.* **2023**, *123*, 1–30. [CrossRef]
10. Oshima, T.; Nishioka, S.; Kikuchi, Y.; Hirai, S.; Yanagisawa, K.; Eguchi, M.; Maeda, K. An Artificial Z-Scheme Constructed from Dye-Sensitized Metal Oxide Nanosheets for Visible Light-Driven Overall Water Splitting. *J. Am. Chem. Soc.* **2020**, *142*, 8412–8420. [CrossRef]
11. Jin, X.X.; Wang, R.Y.; Zhang, L.X.; Si, R.; Shen, M.; Wang, M.; Tian, J.J.; Shi, J.L. Electron Configuration Modulation of Nickel Single Atoms for Elevated Photocatalytic Hydrogen Evolution. *Angew. Chem. Int. Ed.* **2020**, *59*, 6827–6831. [CrossRef]
12. Zhu, Q.H.; Xu, Q.; Du, M.M.; Zeng, X.F.; Zhong, G.F.; Qiu, B.C.; Zhang, J.L. Recent progress of metal sulfide photocatalysts for solar energy conversion. *Adv. Mater.* **2022**, *34*, 2202929. [CrossRef]
13. Zhang, F.; Li, J.M.; Wang, H.F.; Li, Y.P.; Liu, Y.; Qian, Q.; Zhang, G. Realizing Synergistic Effect of Electronic Modulation and Nanostructure Engineering over Graphitic Carbon Nitride for Highly Efficient Visible-Light H_2 Production Coupled with Benzyl Alcohol Oxidation. *Appl. Catal. B Environ.* **2020**, *269*, 118772. [CrossRef]
14. Meng, S.; Ye, X.; Zhang, J.; Fu, X.; Chen, S. Effective use of photogenerated electrons and holes in a system: Photocatalytic selective oxidation of aromatic alcohols to aldehydes and hydrogen production. *J. Catal.* **2018**, *367*, 159–170. [CrossRef]
15. Zong, X.; Yan, H.H.; Wu, G.P.; Ma, G.J.; Wen, F.Y.; Wang, L.; Li, C. Enhancement of photocatalytic H_2 evolution on CdS by loading MoS_2 as cocatalyst under visible light irradiation. *J. Am. Chem. Soc.* **2008**, *130*, 7176–7177. [CrossRef]
16. Fazil, M.; Ahmad, T. Pristine TiO_2 and Sr-Doped TiO_2 Nanostructures for Enhanced Photocatalytic and Electrocatalytic Water Splitting Applications. *Catalysts* **2023**, *13*, 93. [CrossRef]
17. AlSalka, Y.; Al-Madanat, O.; Hakki, A.; Bahnemann, D.W. Boosting the H_2 production efficiency via photocatalytic organic reforming: The role of additional hole scavenging system. *Catalysts* **2021**, *11*, 1423. [CrossRef]
18. Al-Madanat, O.; Alsalka, Y.; Curti, M.; Dillert, R.; Bahnemann, D.W. Mechanistic insights into hydrogen evolution by photocatalytic reforming of naphthalene. *ACS Catal.* **2020**, *10*, 7398–7412. [CrossRef]
19. Al-Madanat, O.; AlSalka, Y.; Ramadan, W.; Bahnemann, D.W. TiO_2 photocatalysis for the transformation of aromatic water pollutants into fuels. *Catalysts* **2021**, *11*, 317. [CrossRef]
20. Schneider, J.; Bahnemann, D.W. Undesired role of sacrificial reagents in photocatalysis. *J. Chem. Phys. Lett.* **2013**, *4*, 3479–3483. [CrossRef]
21. Zhou, P.; Lv, F.; Li, N.; Zhang, Y.L.; Mu, Z.J.; Tang, Y.H.; Guo, S. Strengthening reactive metal-support interaction to stabilize high-density Pt single atoms on electron-deficient g-C_3N_4 for boosting photocatalytic H_2 production. *Nano Energy* **2019**, *56*, 127–137. [CrossRef]
22. Ma, X.H.; Li, W.J.; Li, H.D.; Dong, M.; Li, X.Y.; Geng, L.; Wang, T. Fabrication of novel and noble-metal-free MoP/In_2S_3 Schottky heterojunction photocatalyst with efficient charge separation for enhanced photocatalytic H_2 evolution under visible light. *J. Colloid Interf. Sci.* **2022**, *617*, 284–292. [CrossRef]
23. Yang, L.F.; Li, A.Q.; Dang, T.; Wang, Y.F.; Liang, L.; Tang, J.; Zhang, Z. S-scheme In_2S_3/$Zn_3In_2S_6$ microsphere for efficient photocatalytic H_2 evolution with simultaneous photodegradation of bisphenol A. *Appl. Surf. Sci.* **2023**, *612*, 155848. [CrossRef]
24. Zhang, R.Y.; Jia, X.W.; Li, Y.R.; Yu, X.D.; Xing, Y. Oxidation co-catalyst modified In_2S_3 with efficient interfacial charge transfer for boosting photocatalytic H_2 evolution. *Int. J. Hydrogen Energ.* **2022**, *47*, 25300–25308. [CrossRef]
25. Lin, Q.C.; Li, Z.H.; Lin, T.J.; Li, B.L.; Liao, X.C.; Yu, H.Q.; Yu, C.L. Controlled preparation of P-doped g-C_3N_4 nanosheets for efficient photocatalytic hydrogen production. *Chin. J. Chem. Eng.* **2020**, *28*, 2677–2688. [CrossRef]
26. Chen, X.B.; Shen, S.H.; Guo, L.J.; Mao, S.S. Semiconductor-based photocatalytic hydrogen generation. *Chem. Rev.* **2010**, *110*, 6503–6570. [CrossRef]
27. Chai, Z.G.; Zeng, T.T.; Li, Q.; Lu, L.Q.; Xiao, W.J.; Xu, D.S. Efficient visible light-driven splitting of alcohols into hydrogen and corresponding carbonyl compounds over a Ni-modified CdS photocatalyst. *J. Am. Chem. Soc.* **2016**, *138*, 10128–10131. [CrossRef]
28. Xiong, Z.; Hou, Y.D.; Yuan, R.S.; Ding, Z.X.; Ong, W.J.; Wang, S.B. Hollow $NiCo_2S_4$ nanospheres as a cocatalyst to support $ZnIn_2S_4$ nanosheets for visible-light-driven hydrogen production. *Acta. Phys.-Chim. Sin.* **2022**, *38*, 2111021.
29. Li, S.C.; Shi, M.Y.; Yu, J.H.; Li, S.J.; Lei, S.L.; Lin, L.G.; Wang, J.J. Two-dimensional blue-phase CX (X = S, Se) monolayers with high carrier mobility and tunable photocatalytic water splitting capability. *Chin. Chem. Lett.* **2021**, *32*, 1977–1982. [CrossRef]
30. Yuan, L.; Li, Y.H.; Tang, Z.R.; Gong, J.L.; Xu, Y.J. Defect-promoted visible light-driven CC coupling reactions pairing with CO_2 reduction. *J. Catal.* **2020**, *390*, 244–250. [CrossRef]
31. Meng, S.; Wu, H.; Cui, Y.; Zheng, X.; Wang, H.; Chen, S.; Fu, X. One-step synthesis of 2D/2D-3D NiS/$Zn_3In_2S_6$ hierarchical structure toward solar-to-chemical energy transformation of biomass-relevant alcohols. *Appl. Catal. B Environ.* **2020**, *266*, 118617. [CrossRef]
32. Qi, M.Y.; Conte, M.; Anpo, M.; Tang, Z.R.; Xu, Y.J. Cooperative coupling of oxidative organic synthesis and hydrogen production over semiconductor-based photocatalysts. *Chem. Rev.* **2021**, *121*, 13051–13085. [CrossRef]
33. Fu, X.; Zhang, L.; Liu, L.; Li, H.; Meng, S.; Ye, X.; Chen, S. In situ photodeposition of MoS_x on CdS nanorods as a highly efficient cocatalyst for photocatalytic hydrogen production. *J. Mater. Chem. A* **2017**, *5*, 15287–15293. [CrossRef]

34. Shen, R.C.; Ren, D.D.; Ding, Y.N.; Guan, Y.T.; Ng, Y.H.; Zhang, P.; Li, X. Nanostructured CdS for efficient photocatalytic H_2 evolution: A review. *Sci. China Mater.* **2020**, *63*, 2153–2188. [CrossRef]
35. Li, L.; Guo, C.F.; Ning, J.Q.; Zhong, Y.J.; Chen, D.L.; Hu, Y. Oxygen-vacancy-assisted construction of FeOOH/CdS heterostructure as an efficient bifunctional photocatalyst for CO_2 conversion and water oxidation. *Appl. Catal. B Environ.* **2021**, *293*, 120203. [CrossRef]
36. Han, G.Q.; Jin, Y.H.; Burgess, R.A.; Dickenson, N.E.; Cao, X.M.; Sun, Y.J. Visible-Light-Driven Valorization of Biomass Intermediates Integrated with H_2 Production Catalyzed by Ultrathin Ni/CdS Nanosheets. *J. Am. Chem. Soc.* **2017**, *139*, 15584–15587. [CrossRef]
37. Liu, M.C.; Chen, Y.B.; Su, J.Z.; Shi, J.W.; Wang, X.X.; Guo, L.J. Photocatalytic Hydrogen Production using Twinned Nanocrystals and an Unanchored NiS_x Co-Catalyst. *Nat. Energy* **2016**, *1*, 16151. [CrossRef]
38. Li, S.J.; Cai, M.J.; Liu, Y.P.; Wang, C.C.; Yan, R.Y.; Chen, X.B. Constructing $Cd_{0.5}Zn_{0.5}S/Bi_2WO_6$ S-scheme heterojunction for boosted photocatalytic antibiotic oxidation and Cr(VI) reduction. *Adv. Powder Mater.* **2023**, *2*, 100073. [CrossRef]
39. Dong, Y.J.; Han, Q.; Hu, Q.Y.; Xu, C.J.; Dong, C.Z.; Peng, Y.; Lan, Y. Carbon quantum dots enriching molecular nickel polyoxometalate over CdS semiconductor for photocatalytic water splitting. *Appl. Catal. B* **2021**, *293*, 120214. [CrossRef]
40. Ye, H.F.; Shi, R.; Yang, X.; Fu, W.F.; Chen, Y. P-doped $Zn_xCd_{1-x}S$ solid solutions as photocatalysts for hydrogen evolution from water splitting coupled with photocatalytic oxidation of 5-hydroxymethylfurfural. *Appl. Catal. B Environ.* **2018**, *233*, 70–79. [CrossRef]
41. Yang, Y.; Ren, W.; Zheng, X.; Meng, S.; Cai, C.; Fu, X.; Chen, S. Decorating $Zn_{0.5}Cd_{0.5}S$ with C, N Co-Doped CoP: An Efficient Dual-Functional Photocatalyst for H_2 Evolution and 2,5-Diformylfuran Oxidation. *ACS Appl. Mater. Inter.* **2022**, *14*, 54649–54661. [CrossRef]
42. Zhu, Z.; Zhang, S.; Chen, G.; Meng, S.; Zheng, X.; Chen, S.; Zhang, F. Minimized Pt deposition on CdS simultaneously maximizes the performance of hydrogen production and aromatic alcohols oxidation. *Appl. Surf. Sci.* **2021**, *564*, 150446. [CrossRef]
43. Shi, X.W.; Dai, C.; Wang, X.; Hu, J.Y.; Zhang, J.Y.; Zheng, L.; Zhu, M. Protruding Pt single-sites on hexagonal $ZnIn_2S_4$ to accelerate photocatalytic hydrogen evolution. *Nat. Commun.* **2022**, *13*, 1287. [CrossRef]
44. Andreou, E.K.; Koutsouroubi, E.D.; Vamvasakis, I.; Armatas, G.S. Ni2P-modified P-Doped Carbon Nitride Hetero-Nanostructures for Efficient Photocatalytic Aqueous Cr(VI) Reduction. *Catalysts* **2023**, *13*, 437. [CrossRef]
45. Yang, Y.; Zheng, X.Z.; Liu, J.F.; Qi, Z.L.; Su, T.Y.; Cai, C.; Chen, S. Efficient H_2 evolution on $Co_3S_4/Zn_{0.5}Cd_{0.5}S$ nanocomposites by photocatalytic synergistic reaction. *Inorg. Chem. Front.* **2022**, *9*, 1943–1955. [CrossRef]
46. Shen, R.C.; Ding, Y.N.; Li, S.B.; Zhang, P.; Xiang, Q.J.; Ng, Y.H.; Li, X. Constructing low-cost Ni_3C/twin-crystal $Zn_{0.5}Cd_{0.5}S$ heterojunction/ homojunction nanohybrids for efficient photocatalytic H_2 evolution. *Chin. J. Catal.* **2021**, *42*, 25–36. [CrossRef]
47. Li, K.; Chai, B.; Peng, T.Y.; Mao, J.; Zan, L. Preparation of $AgIn_5S_8/TiO_2$ heterojunction nanocomposite and its enhanced photocatalytic H_2 production property under visible light. *ACS Catal.* **2013**, *3*, 170–177. [CrossRef]
48. He, Y.; Li, D.; Xiao, G.; Chen, W.; Chen, Y.; Sun, M.; Huang, H.; Fu, X. A New Application of Nanocrystal In_2S_3 in Efficient Degradation of Organic Pollutants under Visible Light Irradiation. *J. Phys. Chem. C* **2009**, *113*, 5254–5262. [CrossRef]
49. Sun, X.; Luo, X.; Zhang, X.; Xie, J.; Jin, S.; Wang, H.; Zheng, X.; Wu, X.; Xie, Y. Enhanced Superoxide Generation on Defective Surfaces for Selective Photooxidation. *J. Am. Chem. Soc.* **2019**, *141*, 3797–3801. [CrossRef]
50. Li, T.; Zhang, S.; Meng, S.; Ye, X.; Fu, X.; Chen, S. Amino acid-assisted synthesis of In_2S_3 hierarchical architectures for selective oxidation of aromatic alcohols to aromatic aldehydes. *RSC Adv.* **2017**, *7*, 6457–6466. [CrossRef]
51. Meng, S.; Ye, X.; Ning, X.; Xie, M.; Fu, X.; Chen, S. Selective oxidation of aromatic alcohols to aromatic aldehydes by BN/metal sulfide with enhanced photocatalytic activity. *Appl. Catal. B Environ.* **2016**, *182*, 356–368. [CrossRef]
52. Meng, S.; Cui, Y.; Wang, H.; Zheng, X.; Fu, X.; Chen, S. Noble metal-free 0D-1D NiS_x/CdS nanocomposites toward highly efficient photocatalytic contamination removal and hydrogen evolution under visible light. *Dalton T.* **2018**, *47*, 12671–12683. [CrossRef]
53. Cheng, T.T.; Gao, H.J.; Liu, G.R.; Pu, Z.S.; Wang, S.F.; Yi, Z.; Yang, H. Preparation of core-shell heterojunction photocatalysts by coating CdS nanoparticles onto $Bi_4Ti_3O_{12}$ hierarchical microspheres and their photocatalytic removal of organic pollutants and Cr (VI) ions. *Colloid. Surf. A* **2022**, *633*, 127918. [CrossRef]
54. Li, W.J.; Lin, Z.Y.; Yang, G.W. A 2D self-assembled $MoS_2/Znln_2S_4$ heterostructure for efficient photocatalytic hydrogen evolution. *Nanoscale* **2017**, *9*, 18290–18298. [CrossRef]
55. Pasupuleti, K.S.; Reddeppa, M.; Park, B.-G.; Oh, J.-E.; Kim, S.-G.; Kim, M.-D. Efficient Charge Separation in Polypyrrole/GaN-Nanorod-Based Hybrid Heterojunctions for High-Performance Self-Powered UV Photodetection. *Phys. Status Solidi-Rapid Res. Lett.* **2021**, *15*, 2000518. [CrossRef]
56. Wu, H.; Meng, S.; Zhang, J.; Zheng, X.; Wang, Y.; Chen, S.; Fu, X. Construction of two-dimensionally relative p-n heterojunction for efficient photocatalytic redox reactions under visible light. *Appl. Surf. Sci.* **2020**, *505*, 144638. [CrossRef]
57. Deng, H.Z.; Fei, X.G.; Yang, Y.; Fan, J.J.; Yu, J.G.; Cheng, B.; Zhang, L.Y. S-scheme heterojunction based on p-type $ZnMn_2O_4$ and n-type ZnO with improved photocatalytic CO_2 reduction activity. *Chem. Eng. J.* **2021**, *409*, 127377. [CrossRef]
58. Liu, D.N.; Chen, D.Y.; Li, N.J.; Xu, Q.F.; Li, H.; He, J.H.; Lu, J.M. Surface engineering of $g-C_3N_4$ by stacked BiOBr sheets rich in oxygen vacancies for boosting photocatalytic performance. *Angew. Chem. Int. Ed.* **2020**, *59*, 4519–4524. [CrossRef]
59. Yang, W.L.; Zhang, L.; Xie, J.F.; Zhang, X.D.; Liu, Q.H.; Yao, T.; Xie, Y. Enhanced photoexcited carrier separation in oxygen-doped $ZnIn_2S_4$ nanosheets for hydrogen evolution. *Angew. Chem. Int. Edit.* **2016**, *55*, 6716–6720. [CrossRef]

60. Nielsen, M.; Kammer, A.; Cozzula, D.; Junge, H.; Gladiali, S.; Beller, M. Efficient hydrogen production from alcohols under mild reaction conditions. *Angew. Chem., Int. Ed.* **2011**, *50*, 9593. [CrossRef]
61. Zheng, X.Z.; Zhang, Z.; Meng, S.; Wang, Y.X.; Li, D. Regulating charge transfer over 3D Au/ZnO hybrid inverse opal toward efficiently photocatalytic degradation of bisphenol A and photoelectrochemical water splitting. *Chem. Eng. J.* **2020**, *393*, 124676. [CrossRef]
62. Khan, I.; Saeed, K.; Ali, N.; Khan, I.; Zhang, B.; Sadiq, M. Heterogeneous photodegradation of industrial dyes: An insight to different mechanisms and rate affecting parameters. *J. Environ. Chem. Eng.* **2020**, *8*, 104364. [CrossRef]
63. Ahmad, S.; Almehmadi, M.; Janjuhah, H.T.; Kontakiotis, G.; Abdulaziz, O.; Saeed, K.; Ahmad, H.; Allahyani, M.; Aljuaid, A.; Alsaiari, A.A.; et al. The Effect of Mineral Ions Present in Tap Water on Photodegradation of Organic Pollutants: Future Perspectives. *Water* **2023**, *15*, 175. [CrossRef]
64. Al-Madanat, O.; AlSalka, Y.; Dillert, R.; Bahnemann, D.W. Photocatalytic H_2 production from naphthalene by various TiO_2 photocatalysts: Impact of Pt loading and formation of intermediates. *Catalysts* **2021**, *11*, 107. [CrossRef]
65. Al-Madanat, O.; Curti, M.; Günnemann, C.; AlSalka, Y.; Dillert, R.; Bahnemann, D.W. TiO_2 photocatalysis: Impact of the platinum loading method on reductive and oxidative half-reactions. *Catal. Today* **2021**, *380*, 3–15. [CrossRef]
66. Pasupuleti, K.S.; Chougule, S.S.; Jung, N.; Yu, Y.J.; Oh, J.-E.; Kim, M.-D. Plasmonic Pt nanoparticles triggered efficient charge separation in TiO_2/GaN NRs hybrid heterojunction for the high performance self-powered UV photodetectors. *Appl. Surf. Sci.* **2022**, *594*, 153474. [CrossRef]
67. Pasupuleti, K.S.; Reddeppa, M.; Park, B.-G.; Peta, K.R.; Oh, J.-E.; Kim, S.-G.; Kim, M.-D. Ag nanowire-plasmonic-assisted charge separation in hybrid heterojunctions of Ppy-PEDOT: PSS/GaN nanorods for enhanced UV photodetection. *ACS Appl. Mater. Interfaces* **2020**, *12*, 54181–54190. [CrossRef]
68. Wan, J.; Liu, L.; Wu, Y.; Song, J.R.; Liu, J.Q.; Song, R.; Xiong, Y. Exploring the polarization photocatalysis of $ZnIn_2S_4$ material toward hydrogen evolution by integrating cascade electric fields with hole transfer vehicle. *Adv. Funct. Mater.* **2022**, *32*, 2203252. [CrossRef]
69. Wan, J.; Yang, W.J.; Liu, J.Q.; Sun, K.L.; Liu, L.; Fu, F. Enhancing an internal electric field by a solid solution strategy for steering bulk-charge flow and boosting photocatalytic activity of $Bi_{24}O_{31}Cl_xBr_{10-x}$. *Chin. J. Catal.* **2022**, *43*, 485–496. [CrossRef]
70. Hu, Z.F.; Yuan, L.Y.; Liu, Z.F.; Shen, Z.R.; Yu, J.C. An Elemental Phosphorus Photocatalyst with a Record High Hydrogen Evolution Efficiency. *Angew. Chem. Int. Ed.* **2016**, *55*, 9793. [CrossRef]
71. Pasupuleti, K.S.; Ghosh, S.; Jayababu, N.; Kang, C.J.; Cho, H.D.; Kim, S.-G.; Kim, M.-D. Boron doped g-C_3N_4 quantum dots based highly sensitive surface acoustic wave NO_2 sensor with faster gas kinetics under UV light illumination. *Sensor. Actuat. B Chem.* **2023**, *378*, 133140. [CrossRef]
72. Nowicka, E.; Hofmann, J.P.; Parker, S.F.; Sankar, M.; Lari, G.M.; Kondrat, S.A.; Knight, D.W.; Bethell, D.; Weckhuysen, B.M.; Hutchings, G.J. In situ spectroscopic investigation of oxidative dehydrogenation and disproportionation of benzyl alcohol. *Phys. Chem. Chem. Phys.* **2013**, *15*, 12147–12155. [CrossRef]
73. Sun, Z.; Yang, X.; Yu, X.-F.; Xia, L.; Peng, Y.; Li, Z.; Zhang, Y.; Cheng, J.; Zhang, K.; Yu, J. Surface oxygen vacancies of Pd/Bi_2MoO_{6-x} acts as "Electron Bridge" to promote photocatalytic selective oxidation of alcohol. *Appl. Catal. B Environ.* **2021**, *285*, 119790. [CrossRef]
74. Al-Madanat, O.; Nunes, B.N.; AlSalka, Y.; Hakki, A.; Curti, M.; Patrocinio, A.O.T.; Bahnemann, D.W. Application of EPR spectroscopy in TiO_2 and Nb_2O_5 photocatalysis. *Catalysts* **2021**, *11*, 1514. [CrossRef]
75. Chen, Z.X.; Li, D.Z.; Zhang, W.J.; Chen, C.; Li, W.J.; Sun, M.; Fu, X. Low-temperature and template-free synthesis of $ZnIn_2S_4$ microspheres. *Inorg. Chem.* **2008**, *47*, 9766–9772. [CrossRef]